Magnon squeezing in antiferromagnetic MnF_2 and FeF_2

Jimin Zhao,* A. V. Bragas,† and R. Merlin
Focus Center and Department of Physics, University of Michigan, Ann Arbor, Michigan 48109-1040, USA

D. J. Lockwood‡
Institute for Microstructural Sciences, National Research Council, Ottawa, Ontario K1A 0R6, Canada
(Received 20 February 2006; published 25 May 2006)

Quantum squeezing of a collective spin-wave excitation or magnon using femtosecond optical pulses has been used to generate correlated pairs of spins with equal and opposite wave vectors in antiferromagnetic MnF_2 and FeF_2. In the squeezed state, the fluctuations of the magnetization of a crystallographic unit cell vary periodically in time and are reduced below that of the ground state quantum noise. The results obtained, including their temperature dependence for FeF_2, are compared with earlier spontaneous Raman scattering measurements. The squeezing effect is observed to be at least one order of magnitude stronger in FeF_2 than in MnF_2.

DOI: 10.1103/PhysRevB.73.184434 PACS number(s): 75.90.+w, 78.47.+p, 42.65.Dr, 42.50.Dv

I. INTRODUCTION

Quantum squeezing relates to the reduction of the quantum noise of a physical system to below the standard quantum limit. In quantum mechanics, for a given observable, O, the quantum noise is defined as $\Delta O=\sqrt{\langle O^2\rangle-\langle O\rangle^2}$, where the expectation values in the equation are, as usual, defined as $\langle O\rangle=\langle\psi|O|\psi\rangle/\langle\psi|\psi\rangle$. Quantum noise distinguishes itself from classical noise by obeying the Heisenberg uncertainty principle. In 1927, Heisenberg postulated that the quantum noise of conjugate variables A and B (conjugate variables obey the relation $[A,B]=i\hbar$) obeys the relation $\Delta A\Delta B \geq \hbar/2$.[1] The uncertainty principle shows that there is a limitation on eliminating the quantum noise of both A and B simultaneously. Therefore, noise is intrinsic to a physical system; even after the classical thermal noise is eliminated from a system, at a sufficiently low temperature, quantum noise still exists due to the quantum uncertainty principle. Remarkably, despite this fact, the noise of a *given* quantum observable can, in theory, be reduced without limitation through quantum squeezing.[2] Quantum squeezing refers to a state where the noise in one variable has been reduced at the expense of enhancing the noise of its conjugate variable.

The terminology "squeezing" originates from quantum optics and is usually applied to a system of noninteracting bosons. Squeezed states have only been achieved experimentally fairly recently and were first demonstrated for the electromagnetic field (photons) in 1985.[3] Nonlinear interactions of light with passive and active atomic media have been successfully used to generate squeezed photons, opening possibilities for essentially noiseless optical communications and precision measurements (see Refs. 4 and 5, and references therein). Since then, squeezed states have also been realized in other systems. In the past decade, squeezed states of vibrational degrees of freedom have been experimentally demonstrated for molecules[6] and solids,[7–10] and, more recently, squeezed atomic spin states have also been achieved.[11–15] Because spin squeezing is closely related to quantum entanglement, squeezed states hold promise for applications in quantum computing.[16] In addition, thermal squeezing is also possible for classical objects.[17]

Here we concern ourselves with the noise in a magnetically ordered solid for which the low-lying spin excitations are quanta associated with spin waves.[18] Consider a magnetic crystal where the electronic spins associated with the lattice ions are spatially ordered at low temperature. In the ground state, the spins are fully aligned so that the total energy is minimized. In the excited states, the spins deviate from their individual equilibrium values, and the spin system is well described by the superposition of different modes of spin waves (the normal modes are determined by the spin Hamiltonian). The quanta of such spin waves are known as magnons, which are weakly interacting bosons. These low-energy elementary excitations only exist at temperatures below the magnetic ordering temperature. In a recent work, we reported the first experimental demonstration of the generation of squeezed spin-wave states in antiferromagnetic MnF_2.[19] The squeezing mechanism in this case is two-magnon impulsive stimulated Raman scattering (ISRS).

Impulsive stimulated second-order inelastic light scattering has been shown previously to be a practical means of generating squeezed states for phonons in solids.[7–10,20] Second-order Raman coupling between the incident light and lattice vibrations is proportional to the square of the phonon amplitude. The light-induced interaction between a pair of phonons gives rise to squeezing because it results in a change in the frequency of the harmonic oscillator for the duration of the incident light pulse and, as such, it is a parametric perturbation. Here we use an analogous method to achieve squeezed states for magnons. Like phonons, magnons are also low-lying collective excitations, and have been commonly observed by spontaneous Raman scattering (RS).[18] Unlike spontaneous RS, ISRS allows the excitation of *coherent* magnon states—and hence their superposition—for which the phase is well defined. Note that all squeezed states are coherent and have well-defined phases.

For noninteracting bosonic systems, that is, in the harmonic approximation, the ground state of the Hamiltonian is an eigenstate that does not evolve with time. A squeezed state is not an eigenstate, but a superposition of eigenstates. Therefore, a squeezed state will evolve with time. For this time-varying superposition of the eigenstates, the noise of the given observable is periodically modified. Our experi-

ments have shown that magnon squeezing in antiferromagnets results in a periodic reduction of the noise of the crystallographic unit cell magnetization and the frequency of noise reduction is twice the frequency of the magnon oscillation.

Spontaneous RS studies have shown that, in MnF_2, FeF_2, and many other antiferromagnets, the integrated intensity of one magnon RS is smaller than the two-magnon RS. The one-magnon RS is based on a spin-orbit coupling mechanism whereas the two-magnon RS is a result of a unique excited-state exchange interaction involving a pair of magnons that propagate in opposite directions on the two interpenetrating magnetic sublattices.[21] As a result of this mechanism, strong two-magnon RS is found in antiferromagnetic crystals as compared with ferromagnetic materials where the spin-orbit coupling mechanism operates in second order. The strong two-magnon RS in antiferromagnets allows us to obtain clear results regarding the generation of squeezed magnon states.

In Sec. II, we provide details of the theory of two-magnon ISRS and the squeezing mechanism. In Sec. III, we give details of the experimental arrangement and present results for MnF_2 and FeF_2. In Sec. IV, we discuss the results and make comparisons with previous work and, finally, in Sec. V, present our conclusions.

II. THE SQUEEZING MECHANISM AND TWO-MAGNON ISRS

A. Generation of squeezed magnon states

Manganese difluoride and FeF_2 are amongst the simplest of antiferromagnetic insulators.[18] They both crystallize in the rutile structure of D_{4h} point group symmetry. Below the ordering (Néel) temperature they become antiferromagnetic, and the point group for the spatially ordered electronic spins associated with the lattice ions becomes D_{2h}. Manganese difluoride has a Néel temperature $T_N=68$ K (Ref. 22) and electronic spin $S=5/2$ while FeF_2 has a Néel temperature of 78.4 K and $S=2$. In the ordered state at low temperature, the Mn^{2+} (Fe^{2+}) spins align "up" and "down" alternately along the fourfold $[001]$ z axis. The spins aligned "up" form a spin sublattice α and the spins aligned "down" form a spin sublattice β. The two sublattices are interpenetrating, and they together form the overall antiferromagnetic spin arrangement.[21]

Ignoring the weaker intrasublattice exchange interactions J_1 and J_3 (here 1 and 3 refer to the nearest and third-nearest magnetic ion neighbors) and the magnetic anisotropy H_A, the spin dynamics of MnF_2 and FeF_2 is well described by the one-parameter Hamiltonian,[18,21]

$$H_0 = J\sum_{\langle u,v\rangle} \mathbf{S}_{u,\alpha}\cdot\mathbf{S}_{v,\beta}, \tag{1}$$

where $J=J_2$ is the dominant intersublattice antiferromagnetic exchange constant associated with the interaction between a given Mn^{2+} (Fe^{2+}) ion and its eight next-nearest neighbors. Here u and v are used to label ions on sublattices α and β, respectively, and the sum runs over all pairs of next-nearest neighbors. Note that all next-nearest neighbor ions reside on the opposite sublattice. The Hamiltonian in Eq. (1) is expressed in terms of spins. In the harmonic approximation, we can re-express the Hamiltonian in terms of magnon operators[23] as

$$H_0 = \sum_{\mathbf{q}} \hbar\,\Omega_{\mathbf{q}}(a^{\dagger}_{\uparrow\mathbf{q}}a_{\uparrow\mathbf{q}} + a^{\dagger}_{\downarrow\mathbf{q}}a_{\downarrow\mathbf{q}}), \tag{2}$$

where $a^{\dagger}_{\uparrow\mathbf{q}}$ and $a^{\dagger}_{\downarrow\mathbf{q}}$ ($a_{\uparrow\mathbf{q}}$ and $a_{\downarrow\mathbf{q}}$) are creation (annihilation) operators for magnons of wave vector $\mathbf{q}$ and frequency $\Omega_{\mathbf{q}}$ belonging to the two degenerate branches labeled $\uparrow$ and $\downarrow$.[21,24] The degeneracy can be lifted by an external magnetic field and, for wave vectors near the edge of the Brillouin zone, the excitations generated by $a^{\dagger}_{\uparrow\mathbf{q}}$ ($a^{\dagger}_{\downarrow\mathbf{q}}$) propagate mainly on the α (β) sublattice (a magnon of arbitrary $\mathbf{q}$ generally perturbs both sublattices).[18]

Phenomenologically, the Raman coupling between magnons and light can be expanded in powers of the spins of the magnetic ions.[5] Ordinarily, due to the perturbation nature of the scattering terms, the higher the order of the scattering term, the weaker the scattering intensity. In MnF_2 and FeF_2, however, the first- and second-order contributions relying on spin-orbit coupling are much less significant than the second-order term resulting from the excited-state exchange interaction that involves electric-dipole transitions.[21,24,25] From symmetry considerations, the two-magnon interaction relevant to impulsive RS can be written as[21,24]

$$V = \frac{E^2}{2}\sum_{\langle u,v\rangle} \Xi(u,v)(S^{+}_{u,\alpha}S^{-}_{v,\beta} + S^{-}_{u,\alpha}S^{+}_{v,\beta} + \gamma S^{z}_{u,\alpha}S^{z}_{v,\beta}), \tag{3}$$

where $S^{\pm}=S_x\pm iS_y$, γ is an anisotropy parameter, and

$$\Xi(u,v) = \kappa_1(e_xe_x + e_ye_y) + \kappa_2 e_ze_z + 2\kappa_3(e_xe_y\ \mathrm{sgn}\ \rho_x\ \mathrm{sgn}\ \rho_y) + 2\kappa_4(e_xe_z\ \mathrm{sgn}\ \rho_x\ \mathrm{sgn}\ \rho_z + e_ye_z\ \mathrm{sgn}\ \rho_y\ \mathrm{sgn}\ \rho_z). \tag{4}$$

Here $\mathbf{E}(\mathbf{r},t)=E(e_x,e_y,e_z)$ is the position- and time-dependent electric field, $\boldsymbol{\rho}=\mathbf{r}_u-\mathbf{r}_v=(\rho_x,\rho_y,\rho_z)$ is a real space vector connecting a given ion with its eight next-nearest neighbors, and κ_m ($m=1,2,\ldots,4$) are magneto-optic coefficients[18] associated with the Raman tensors R of symmetry A_{1g} (κ_1 and κ_2), B_{2g} (κ_3), and E_g (κ_4) (see Appendix A). The relative magnitudes of the latter can be inferred from spontaneous Raman data and are shown in Table I. In our experiments we use the xy geometry, where the laser beams are polarized in the xy plane. Therefore the κ_2 and κ_4 terms do not contribute to the scattering. Furthermore, for two-magnon Raman scattering, it is sufficient to consider only zone-edge excitations, because the magnon density of states is strongly peaked at van Hove singularities close to the Brillouin zone boundary. In addition, the coefficient includes a trigonometric term, which has its largest value near the Brillouin zone boundary.

TABLE I. Some physical parameters of antiferromagnetic MnF_2 and FeF_2.

	Néel temperature (K)	Spin	$\lvert\kappa_1/\kappa_3\rvert$	$\lvert\kappa_2/\kappa_3\rvert$	$\lvert\kappa_4/\kappa_3\rvert$	Ref.
MnF_2	68	5/2	0.14	0.32	0.66	24
FeF_2	78.4	2	–	0.3	0.8	28

The commonly observed Raman scattering spectra fully agree with the above arguments. The κ_1 term in Eq. (4) and the term containing γ in Eq. (3) vanish after summation (see Appendix B). Therefore, the only symmetry that matters in our experiments is $B_{2g}(\kappa_3)$.

It is straightforward to express V in terms of magnon operators. Considering mainly zone-edge excitations and writing $V=\Sigma_{\mathbf{q}}V_{\mathbf{q}}$, we obtain for $\mathbf{q}$ near the Brillouin zone edge (see Appendix C),

$$V_{\mathbf{q}} \approx SE^2\Delta_{\mathbf{q}}(a^{\dagger}_{\downarrow\mathbf{q}}a^{\dagger}_{\uparrow-\mathbf{q}} + a_{\downarrow\mathbf{q}}a_{\uparrow-\mathbf{q}}), \tag{5}$$

where the "≈" sign denotes that we consider mainly magnon modes near the zone boundary. The constant S is the spin of Mn^{2+} (Fe^{2+}), and $\Delta_{\mathbf{q}}$ is a weighting factor that generally depends on the field polarization and the appropriate combination of magneto-optic coefficients. For the B_{2g} term, $\Delta_{\mathbf{q}}=-8\kappa_3\sin(q_xa/2)\sin(q_ya/2)\cos(q_zc/2)$, where a and c are the tetragonal lattice constants.[21,24] This geometry favors the M point of the Brillouin zone and it gives the largest contribution to two-magnon RS (see Table I).[21,24]

The coupling defined by V describes a time-dependent pair-wise interaction between magnons. The two magnons forming a pair belong to the two degenerate branches and have wave vectors of equal magnitude but opposite directions. To describe the effect of a laser pulse on the magnetic system, we consider the impulsive limit, i.e., an optical pulse of width $\tau \ll \Omega^{-1}$ and, for simplicity, we take the speed of light $c_L \to \infty$. Then the field can be treated as an instantaneous and position-independent perturbation $E^2 \approx (4\pi I/n_Rc_L)\delta(t)$, where n_R is the refractive index and I is the integrated intensity of the pulse. Let Ψ_0 be the wave function of the whole active region of the crystal just before the pulse strikes. A simple integration of the Schrödinger equation gives, for $t>0$,[7]

$$\Psi(t) = e^{iH_0t/\hbar}\exp\left[-i\sum_{\mathbf{q}}\frac{4\pi SI}{n_Rc_L\hbar}\Delta_{\mathbf{q}}(a^{\dagger}_{\downarrow\mathbf{q}}a^{\dagger}_{\uparrow-\mathbf{q}} + a_{\downarrow\mathbf{q}}a_{\uparrow-\mathbf{q}})\right]\Psi_0. \tag{6}$$

At zero temperature, Ψ_0 is the magnetic ground state and this expression becomes identical to that describing the two-mode squeezed state.[2] After some algebra (see Appendix D), we obtain, to lowest order in the intensity of the pulse,

$$\langle\Psi(t)|(a^{\dagger}_{\downarrow\mathbf{q}}a^{\dagger}_{\uparrow-\mathbf{q}} + a_{\downarrow\mathbf{q}}a_{\uparrow-\mathbf{q}})|\Psi(t)\rangle \approx -\frac{8\pi SI}{n_Rc_L\hbar}\Delta_{\mathbf{q}}\sin(2\Omega_{\mathbf{q}}t). \tag{7}$$

Hence, Eq. (6) represents a state in which there exists a time-varying correlation between magnons of opposite wave vectors that belong to the two degenerate branches. Equation (7) also manifests the coherence of the generated state $\Psi(t)$ after the incidence of the light pulse on the crystal. Equations (6) and (7) indicate that the generated state $\Psi(t)$ is a squeezed magnon state.

To claim that Ψ is a squeezed magnon state, we need to answer the question: What is the magnetic physical quantity that is squeezed, and how does this magnetic physical quantity affect the detection in the experiments? Let $\mathbf{m}_l$ ($l=1,\ldots,N$) be the local magnetization operator for the N crystallographic unit cells. In the following we show that magnon squeezing is tantamount to periodic fluctuations of the noise of the local magnetization $\sigma_m=\sqrt{\langle\mathbf{m}_l^2\rangle}$ (note that $\langle\mathbf{m}_l\rangle=0$ always and that $\langle\mathbf{m}_l^2\rangle$ has the same value for all unit cells).

Writing $\mathbf{m}_l=g\mu_B(\mathbf{S}_{l,\alpha}+\mathbf{S}_{l,\beta})$, where the spins belong to the same unit cell, g is the Landé g factor, and μ_B is the Bohr magneton, we have

$$\frac{1}{2}\sum_l\langle\mathbf{m}_l^2\rangle/(g\mu_B)^2 = NS(S+1) + \sum_{\mathbf{q}}\langle\mathbf{S}_{\alpha}(\mathbf{q})\cdot\mathbf{S}_{\beta}(-\mathbf{q})\rangle, \tag{8}$$

where N is the total number of unit cells and $\mathbf{S}_{\alpha/\beta}(\mathbf{q}) = \Sigma\mathbf{S}_{\alpha/\beta}(\mathbf{r}_{l,\alpha/\beta})\exp(i\mathbf{q}\cdot\mathbf{r}_{l,\alpha/\beta})/N^{1/2}$ (the sum is over all sites of the corresponding sublattice). From Eqs. (6) and (8) with $I \to 0$, we obtain in the harmonic approximation (see Appendix E),

$$\sigma_m(t) \approx \sigma_m(0)\left[1 + \frac{4\pi IS}{Nn_Rc_L\hbar}\sum_{\mathbf{q}}\Delta_{\mathbf{q}}\sin(2\Omega_qt)\right], \tag{9}$$

where $\sigma_m(0)=(2S)^{1/2}g\mu_B$ is the ground state noise, which is associated with the state just before the light pulse arrives. The quantum noise of the cell magnetization after the light pulse is periodically varying. Accordingly, the quantum noise is periodically reduced below that for the ground state. Note that the frequency is twice that of the magnon frequency close to the Brillouin zone boundary.

At this point we give a quantitative estimate of the coupling between the light and the local magnetization noise. We write Eq. (3) as $V=E^2\Sigma_{\mathbf{q}}\Theta(\mathbf{q})\mathbf{S}_{\alpha}(\mathbf{q})\cdot\mathbf{S}_{\beta}(-\mathbf{q})$, which shows that, except for the weighting factors $\Theta(\mathbf{q})$, light couples directly to fluctuations of the local magnetization. Given that contributions near the Brillouin zone boundary are dominant, $V \approx E^2\tilde{\Theta}N\hbar^2[(\sigma_m/g\mu_B)^2/2 - S(S+1)]$ where $\tilde{\Theta}$ denotes an average value at the zone boundary.

B. Detection of squeezed magnon states

Next we focus on the detection of the above squeezed magnon states. The detection of the coherent excited state is an integral part of the pump-probe experiments. Here we detect the squeezed magnon states by measuring the effect of the quantum noise fluctuation in the local magnetization on the intensity of the transmitted probe beam. In our pump-probe experiment, the stronger pump pulse drives the crystal into the time-varying squeezed state [Eq. (6)], in which the corresponding two-magnon impulsive stimulated Raman scattering tensor causes the change of the refractive index (through the generation of the squeezed magnon state, or equivalently, we control the refractive index to generate the squeezed magnon state). The time-varying refractive index then modifies the transmission intensity of the concomitant weaker probe pulse. The signal of interest is the intensity of the transmitted probe beam as a function of the delay time between the two pulses. The controlled delay of the probe beam (relative to the pump pulse) allows us to monitor, in a time-resolved way, the dynamics of the coherent excitation in the crystal. Using Eq. (7) and well-known results for co-

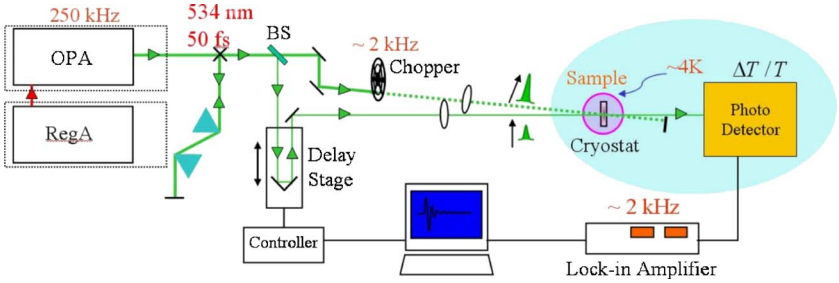

FIG. 1. (Color online) Schematic of the pump-probe experimental arrangement.

herent phonons,[26] we obtain the following expression for the differential transmission:

$$\Delta T/T \approx \frac{\ell I}{\hbar N v_C}\left(\frac{8\pi S}{n_R c_L}\right)^2 \sum_{\mathbf{q}} \Omega_{\mathbf{q}} \Delta_{\mathbf{q}}^2 \cos(2\Omega_{\mathbf{q}} t), \qquad (10)$$

where ℓ is the length of the sample, N is the number of unit cells, and v_C is the cell volume. Equation (10) is valid for probe pulses of negligible width.

The relation between the quantum noise fluctuation in local cell magnetization and the differential transmission can be obtained from Eqs. (9) and (10). Comparison of the two shows that the differential transmission (which is measured in our experiment, as will be shown in Sec. III) is proportional to the change in the noise of the local magnetization, which generates the modification of the refractive index. In essence, the noise is being controlled by the laser-induced refractive index modulation. Explicitly, we have

$$\sigma_m(t) \approx \sigma_m(0)[1 + \xi(\Delta T/T)|_{\max} \sin(2\Omega_M t)], \qquad (11)$$

where $\xi = v_C n_R c_L/(16\pi \ell S \Omega_M \Delta_M)$ is a real coefficient that has a value close to 1. We expect to observe an oscillation in the differential transmission (ΔT) that is at *twice* the frequency of the magnon.

III. EXPERIMENT AND RESULTS

A. Pump-probe experiments

The time-resolved experiments were performed with a fairly standard pump-probe setup, as shown schematically in Fig. 1. The optical sources are tunable visible light pulses from the optical parametric amplifier (OPA), which is pumped at 250 kHz by the 800 nm near infrared pulses from the regenerative amplifier (Coherent RegA). The pulses from the OPA have a tunable central wavelength in the visible range and are compressed with a pair of prisms to compensate for the dispersion caused by the optics inside the OPA and/or from other optics. After compression, the beam is split into two parts: The stronger part is the pump beam and the weaker part is the probe beam. The energy ratio is roughly 4:1 between the pump and probe beams. The delay stage (Newport model UTM150PP1HL with motor UE41PP) is driven by a controller (Newport model ESP300) that is connected to a computer to control the delay time between the pump and the probe beams during the scan. The pump beam is periodically blocked by a chopper (Stanford Research Systems model SR540 chopper) so that the detection is sampled at a fixed frequency (~2 kHz in our experiments). A lock-in amplifier (Stanford Research Systems model SR830 DSP) measures signals only at the preset chopping frequency. Accordingly, higher and lower frequency background noise is filtered out. The characteristic distribution of background noise is such that the higher the frequency, the lower the background noise.

After passing through the sample, the probe beam is detected using a silicon diode photodetector. The voltage signal from the photodetector is first sent to a preamplifier (Stanford Research Systems model SR560), which not only amplifies the signal but also works as a frequency filter. In our experiments, the frequency pass window for detection was set to be 1–3 kHz or 1–10 kHz to observe only the signal at the modulation frequency. The signal coming out of the output of the preamplifier is sent to an oscilloscope to monitor the signal level and also to the lock-in amplifier. The scanning program reads the signal from the lock-in amplifier and it then controls the stepping motor to produce the scanning signal. A CCD camera (Watec America Corp. WAT-902C) is used to observe the focusing and overlap of the pump and probe beams on the sample.

In our experiments, we used two different modifications to the detection scheme (the blue-shaded area in the schematic of Fig. 1). Identical results are obtained from both detection methods. Figure 2 shows the spectrally resolved detection scheme. The transmitted probe beam is dispersed with a grating. In the frequency domain, the probe beam is modulated by the coherent excitation in the sample so that its intensity has a red or blue shift, depending on the delay time between the probe beam and the pump beam. By monitoring the slight difference in the intensities of the two halves, we were able to observe the coherent dynamics inside the sample. Subtraction of the two halves doubles the signal intensity.

The other detection scheme is shown in Fig. 3. The probe beam crosses a half wave plate so that its polarization is

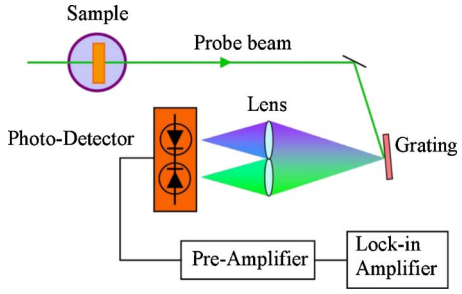

FIG. 2. (Color online) Schematic of the spectrally resolved detection method.

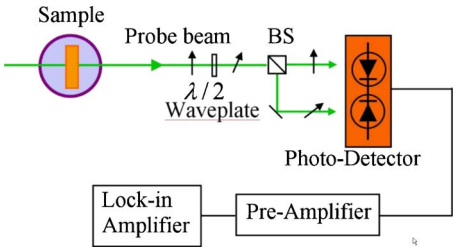

FIG. 3. (Color online) Schematic of the polarization-based detection method.

rotated by an angle that depends on the Raman tensors of the particular mode(s) of interest. In these experiments, the rotation angle was set at 45°. The probe pulse then enters a polarizer cube where it is divided into two nearly equal parts, one part vertically polarized and the other horizontally polarized. The intensity difference between these two halves contains information about the coherent oscillations in the sample.

In the experiments, the samples were cooled by a liquid He flow cryostat (Oxford Instruments Optistat Bath Dynamic Variable Temperature Cryostat, model no. 44090:4) where the sample temperature could be varied from ~3 to 295 K and controlled to within 0.1 K.

B. MnF_2

Data were obtained from a $5.5\times5.8\times6.0$ mm^3 single crystal of MnF_2 grown in the Clarendon Laboratory of Oxford University especially for Raman scattering studies. The crystal boule was x-ray oriented and cut to provide a cuboid sample with diamond-polished faces perpendicular to the crystallographic a, b, and c axes directions, respectively. The sample was of high optical quality and pale-orange in color.[24]

The time-domain measurements were performed at 4 K using a pump-probe transmission geometry that allows excitations of B_{2g} symmetry only to be observed. The crystal was oriented such that the c axis of the crystal was along the laboratory z axis. Light penetrated the crystal along the [001] direction and hence the polarizations of both the pump and probe beams were within the xy plane. We used 50 fs pulses generated by the OPA at the central wavelength of 534 nm, which were focused onto a common 30 μm diameter spot. The average powers for the pump and probe pulses were, respectively, 13 and 3 mW. The pump pulses were polarized along the [110] direction. This geometry couples to modes of both A_{1g} and B_{2g} symmetry, but not for that of E_g and B_{1g} symmetry. The probe polarization was set at an angle of 45° with respect to the polarization of the pump, that is, along the [010] direction. The polarization-based detection method was used to measure the differential transmission (see Fig. 3). After passing through the sample, the transmitted probe pulses were divided into two beams, one polarized parallel and the other one perpendicular to the pump polarization (see Fig. 4). These beams were sent to the two separate detectors. The difference between the signals recorded by these detectors gives the differential transmission for the B_{2g} geometry

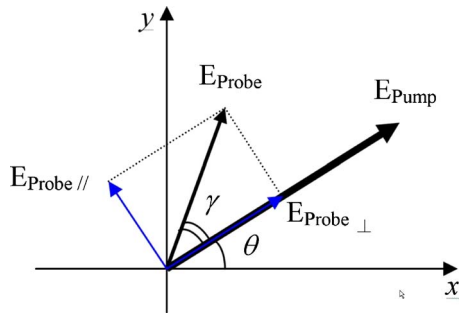

FIG. 4. (Color online) Diagram of the beam polarization configurations in the pump-probe setup. The blue arrows denote the beam polarizations after the cube polarizer shown in Fig. 3.

while the subtraction eliminates the isotropic A_{1g} contribution (see Appendix F).

The time-domain data of Fig. 5(a) show well-resolved oscillations. After removal of the so-called coherent artifact at time $t=0$, we performed a Fourier transform (FT) of the data and the resultant frequency spectrum is plotted in Fig. 5(b). This procedure gives three modes with frequencies of ~100, 347, and 481 cm^{-1}, which are in excellent agreement with those of, respectively, the two-magnon feature and the Raman-allowed phonons of symmetries A_{1g} and B_{2g}.[27] Based on this result and the previous discussion in Sec. II, the ~100 cm^{-1} oscillation is ascribed to the two-magnon squeezed state whereas the other two features are assigned to first-order coherent phonons.[27] The observation of the A_{1g} mode is attributed to a lack of perfect polarization in the experiment. While A_{1g} excitations are not nominally allowed in our xy configuration (see Appendix F), the Raman cross section for the 347 cm^{-1} phonon is so large[27] that it cannot be entirely suppressed by our method.

For comparison with the time-domain produced frequency-domain data, we also measured the spontaneous

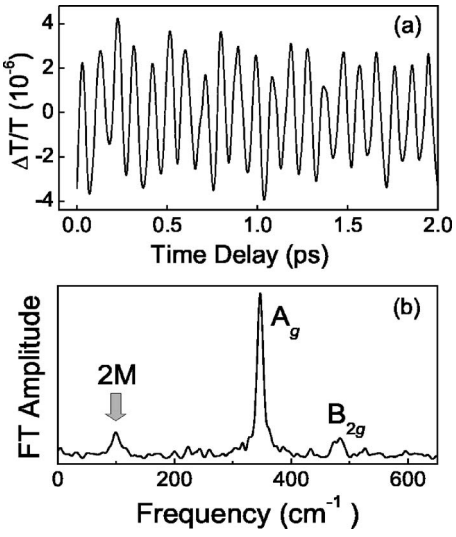

FIG. 5. (a) Time-domain relative differential transmission as a function of pump-probe delay time. (b) The associated Fourier transform (FT) spectrum exhibits peaks due to coherent two-magnon excitations and coherent phonons excited in antiferromagnetic MnF_2 at ~4 K.

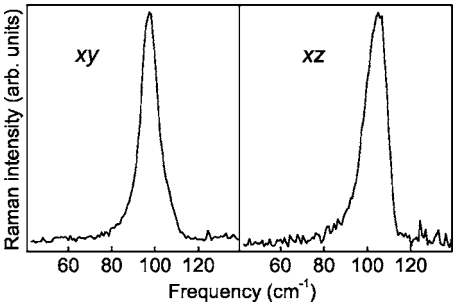

FIG. 6. Spontaneous Raman scattering data for MnF_2 at 3 K. The labels *xy* and *xz* denote the polarization geometries of the two measurements. In order to make a convenient comparison of the line shape, the two curves are plotted such that their maximum intensities are equalized.

Raman scattering of the MnF_2 crystal at ~3 K using 140 mW of 514.5 nm Ar^+ ion laser light. The spectra for the two different geometries *xy* and *xz* are shown in Fig. 6.

C. FeF_2

In order to make a systematic study of the magnon squeezing in different rutile structure materials, we performed a similar experiment in FeF_2. Spontaneous Raman scattering experiments have shown that although one-magnon light scattering in FeF_2 is much stronger than that of MnF_2 the two-magnon scattering is of comparable intensity.[18,24,28] In our experiments on FeF_2, we used the spectrally resolved detection arrangement (see Fig. 2) instead of the polarization-based detection setup used for the MnF_2 experiments.

As for the MnF_2 crystal, pump-probe experiments were performed in the transmission geometry through a 1 mm thick single crystal of FeF_2. The light-brown color sample was oriented, cut, and polished in the way described in Ref. 28. The crystal was oriented so that the *c* axis of the crystal was along the laboratory *z* axis and thus the incident light traversed the crystal along the [001] direction. Pump and probe beam polarizations were parallel to each other and aligned at an angle of 27° from the crystallographic *a* axis (*x* axis). Thus there were both *x*- and *y*-polarized components for both the pump and probe beams. We used 80 fs optical pulses generated by the OPA at the central wavelength of 555 nm: The pump and probe beam powers were 6.2 and 0.7 mW, respectively. The transmitted light detection scheme shown in Fig. 2 was used. Following dispersion, the beam was divided into two parts from the center of the spectrum, and two separate photodiode detectors were used to measure the integrated intensity of the two portions. Subtraction between them was done to remove the dc component and reveal the information on the coherent oscillation. Time-resolved measurements were performed at a series of temperatures ranging from ~3 to 80 K.

In Fig. 7(a) we show the normalized differential transmission as a function of pump-probe delay time for FeF_2 at ~3 K. The Fourier transform of the time-domain trace, as shown in Fig. 7(b), manifests two main oscillation peaks. By comparison with spontaneous Raman spectra,[28] we assign

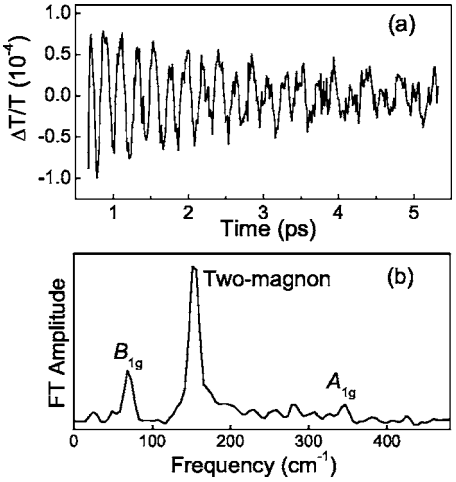

FIG. 7. (a) Normalized differential transmission as a function of pump-probe delay time for FeF_2 at ~3 K. (b) The associated Fourier transform spectrum shows peaks due to coherent two-magnon excitations (squeezed magnons) and coherent phonons.

the peak at 151.3 cm^{-1} to the coherent two-magnon scattering. A coherent phonon mode is also clearly identified, and we assign the peak at 68.3 cm^{-1} to the mode of B_{1g} symmetry.[27] As for MnF_2, the A_{1g} mode is also observed (albeit weakly this time), because of imperfect polarization analysis.

Similar results were obtained in the temperature-dependence study. The time-domain signal strength decreases gradually with increasing temperature, as shown in Fig. 8. The stimulated spin-pair scattering intensity as a function of temperature is also shown in Fig. 8, where the amplitude values have been obtained via the Fourier transform of the time-domain data. When the temperature reaches the

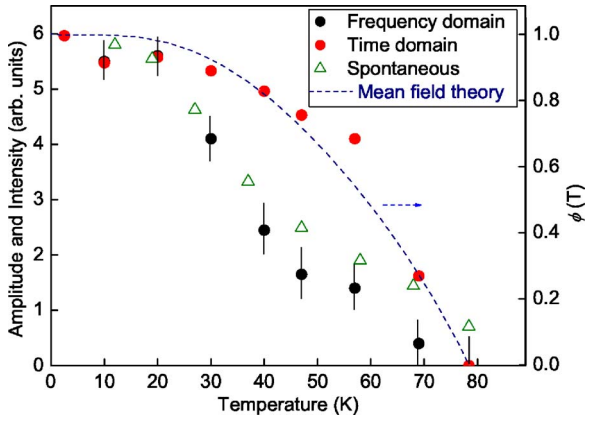

FIG. 8. (Color online) Temperature dependence of the coherent and spontaneous two-magnon Raman scattering intensity in FeF_2. The Fourier transform peak amplitude of the impulsive spin-pair scattering (full black circles) is compared with the previously measured spontaneous Raman scattering peak intensity (open green triangles) (Ref. 28). The full red circles denote the peak-to-peak amplitude of the time-domain signal at ~0.8 ps time delay; the signal clearly vanishes at the Néel temperature of 78.4 K. Also shown is the normalized temperature dependence of the spin-ordering parameter $\varphi(T)$ calculated from mean field theory (blue dashed line) (Ref. 34).

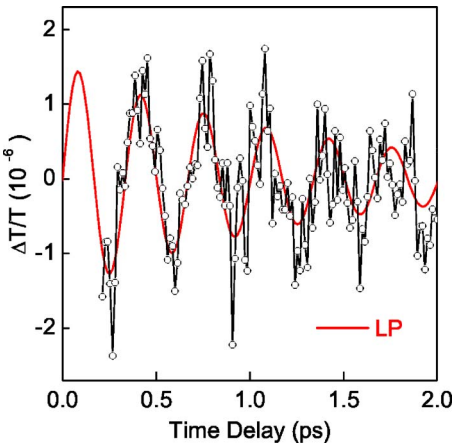

FIG. 9. (Color online) Pump-probe data showing two-magnon oscillations in MnF_2 at 4 K after removal of the phonon oscillation with the linear prediction method. The red line is the linear prediction (LP) model fit.

Néel temperature T_N, the Fourier transform amplitude vanishes (within the measurement error).

IV. DISCUSSION

A. MnF_2

As a parallel approach to simply taking the Fourier transform of the time-domain data, we have also analyzed the time-domain data using linear prediction methods.[29,30] Linear prediction determines directly the number of oscillators and their parameters, including their frequencies, damping rates, phases, and amplitudes. The two-magnon oscillations in MnF_2 are reproduced in Fig. 9 after numerical subtraction of the signal due to the phonons together with the least-squares fit from the linear prediction model.[29,30] As shown in Fig. 10, the Fourier transform of this fit to the time-domain data compares very well with the measured two-magnon spontaneous

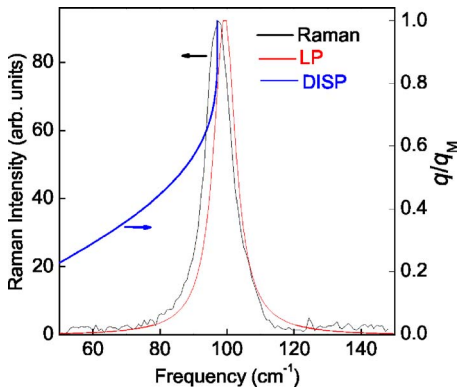

FIG. 10. (Color online) Comparison between the Fourier transform of the linear prediction fit (LP; red trace) and the spontaneous Raman spectrum (black trace) recorded at 3 K in *xy* polarization. The magnon dispersion of MnF_2 for reduced wave vectors in the [110] (*M* point) direction, calculated following Refs. 21 and 22, is shown by the blue trace (DISP). For easy comparison with the Raman experiments, the frequency scale of this dispersion curve has been multiplied by a factor of 2.

Raman spectrum in the *xy* geometry. On the other hand, it is clear from Fig. 6 that the time-domain measurements are not compatible with the spontaneous Raman spectrum in *xz* polarization both with respect to the band position and line shape. In Fig. 10 we also show the [110]-direction magnon dispersion curve for MnF_2 calculated using the dispersion formula and exchange constants given in Refs. 21 and 22, and this supports our contention that the pump-probe signal is dominated by magnon pairs at the Brillouin zone boundary. This dispersion curve together with the comparison with spontaneous Raman spectra[28] confirms that we are indeed coupling to magnons from near the Brillouin zone *M* point, as predicted in Sec. II.

This clear identification of an oscillation at the two-magnon frequency, good comparison with the spontaneous Raman line shape, and agreement with the magnon dispersion curve indicate that we have observed coherent two-magnon light scattering in our pump-probe measurement. From our calculations shown in Sec. II, it can be seen that observing coherent two-magnon light scattering in the pump-probe experiment means that the quantum fluctuations in local cell magnetization have been periodically squeezed. Hence we assert that the coherence responsible for the oscillations of Fig. 9 is that of squeezed magnon states. The magnetic oscillations do not show the phase predicted by Eq. (10) at zero time delay. We believe that this discrepancy reflects the fact that Eq. (3) and, therefore, Eq. (10) apply to transparent materials whereas the wavelength of our laser falls within a broad absorption band of MnF_2.[31] In such a case, it is well-known that the phase of the coherent oscillations can have arbitrary values.[32] Further support for this interpretation is the observation that the two-magnon signal does not vanish in integrated transmission measurements, reflecting the fact that the sample behaves as a frequency-dependent filter.[26]

If, instead of the local magnetization, we use the angle θ defined as $\cos\theta = -\mathbf{S}_{l,\alpha}\cdot\mathbf{S}_{l,\beta}/S(S+1)$ to represent the spin deviation from the perfect spin alignment, the ground state "noise" in terms of θ becomes

$$\sigma_m \approx g\mu_B\sqrt{S(S+1)}\sqrt{\langle\theta^2\rangle}. \tag{12}$$

Thus, pictorially, the laser-excited spin squeezing results in a sinusoidal modulation of $\sqrt{\langle\theta^2\rangle}$, which reflects the laser-induced control over the local magnetization fluctuations. A pictorial representation of the squeezed state induced by the incident light is given in Ref. 33 (see also Fig. 3 in Ref. 19).

By evaluating Eq. (11), one can estimate the noise reduction factor. The thermal noise at 4 K is approximately the product of $\sigma_m(0)$ times twice the Bose factor at $\hbar\Omega_M$.[8] Under our experimental conditions, the term multiplying $\sin(2\Omega_M t)$ in Eq. (11) is $\sim 2\times 10^{-5}$ while the thermal contribution to the noise is $\sim 3\times 10^{-8}$. Hence, at 4 K, the total noise is dominated by quantum fluctuations and the noise level in the local magnetization has been reduced below the standard quantum limit through magnon squeezing.

B. FeF_2

As explained above for the magnon squeezing in MnF_2, our observation of coherent two-magnon oscillations at a

temperature of ~3 K in ISRS indicates that we have also generated squeezed magnon states in FeF_2. From Eq. (11), the squeezing factor is deduced to be $\sim 5\times 10^{-5}$. For comparison, the squeezing factor we observed in MnF_2 was $\sim 2\times 10^{-5}$ (see Sec. IV A). Making allowances for the differences in the FeF_2 and MnF_2 sample thicknesses (1 versus 6 mm) and laser pump and probe powers (6.2 versus 13 mW and 0.7 versus 3 mW, respectively) used in the two experiments yields a squeezing factor for FeF_2 that is approximately 30 times larger than that of MnF_2. From studies of the spontaneous one- and two-magnon RS in FeF_2 and MnF_2,[24,28,34] it is evident that the source of the 1–2 orders of magnitude difference in the squeezing factors observed here for these compounds lies in the absolute values of the magneto-optic coupling coefficients, which in general are not well known.[18] These coefficients are wavelength dependent, and it would be interesting to investigate this aspect further in future experiments.

This stronger scattering in FeF_2 has allowed us to study the temperature dependence of the coherent spin-pair scattering. At temperatures well below the Néel temperature, magnons are well-defined elementary excitations of the magnetically ordered system and, correspondingly, we have observed coherent two-magnon light scattering and squeezed magnon states at specific wave vectors. At higher temperatures approaching the Néel temperature, the magnon dispersion relationship is modified; the magnon concept itself is not such a precise description of the system and the spin excitations become localized. Spontaneous two-magnon RS persists into the paramagnetic phase and can be observed at temperatures well above T_N due to the fact that the zone-edge magnon pairs renormalize more slowly with temperature than do the zero wave vector magnons.[18] At lower temperatures, as can be seen in Fig. 8, the Fourier transform peak amplitude of the coherent scattering compares well with the peak intensity of spontaneous two-magnon RS (the latter data are taken from Figs. 2 and 7 of Ref. 28), but most interestingly, the coherent spin-pair scattering amplitude then falls below that of the spontaneous RS and apparently vanishes as the temperature reaches the Néel temperature (the odd-looking variation with temperature is a result of plotting for signal-to-noise reasons the peak amplitude rather than the area). The vanishing of the coherent two-magnon scattering at T_N is confirmed from measurements of the peak-to-peak amplitude of the oscillations in the time-delay signal, as shown in Fig. 8. Significantly, the temperature dependence of the strength of the time-delay signal follows the same behavior as that of the sublattice spin-ordering parameter.[35] This strongly suggests that longer range spin ordering is an important, if not essential, component of the coherent two-magnon scattering process, which is in contrast with the spontaneous RS case.

V. CONCLUSION

In summary, squeezed magnon (spin-wave) states have been generated using femtosecond optical pulses. The generation mechanism employs two-magnon ISRS. Coherent excitations involving pairs of correlated spins were created by this means in the antiferromagnetic insulators MnF_2 and FeF_2, with the latter demonstrating the strongest squeezing effect. In the squeezed state, the fluctuations of the magnetization of the local crystallographic unit cells vary in time at twice the magnon frequency and are periodically reduced below that of the ground state quantum noise. The temperature dependence of the stimulated spin-pair scattering has also been determined for FeF_2; the ISRS amplitude diminishes and then vanishes as the temperature is raised up to the Néel temperature, which is different from what happens in spontaneous RS.[18]

Spin squeezing of magnetic systems can have significant applications wherever a long coherent lifetime of an ordered spin state is required such as in spintronics and quantum computing.

ACKNOWLEDGMENTS

This work was supported by the NSF under Grants No. PHY 0114336 and DMR 0072897 and by the AFOSR under contract F49620-00-1-0328 through the MURI program.

APPENDIX A

Rutile structure compounds MnF_2 and FeF_2 each have two molecules (six atoms) in their unit cells. Group theory analysis predicts 15 vibrational modes for this crystal structure, of which four are Raman active. The four Raman active symmetries are labeled as A_{1g}, B_{1g}, B_{2g}, and E_g, where the E_g mode is twofold degenerate. The corresponding Raman tensors are[27]

$$R(A_{1g}) = \begin{bmatrix} a & 0 & 0 \\ 0 & a & 0 \\ 0 & 0 & b \end{bmatrix},$$

$$R(B_{1g}) = \begin{bmatrix} c & 0 & 0 \\ 0 & -c & 0 \\ 0 & 0 & 0 \end{bmatrix},$$

$$R(B_{2g}) = \begin{bmatrix} 0 & e & 0 \\ e & 0 & 0 \\ 0 & 0 & 0 \end{bmatrix},$$

and

$$R(E_g) = \begin{bmatrix} 0 & 0 & 0 \\ 0 & 0 & d \\ 0 & d & 0 \end{bmatrix}, \quad \begin{bmatrix} 0 & 0 & d \\ 0 & 0 & 0 \\ d & 0 & 0 \end{bmatrix}. \tag{A1}$$

APPENDIX B

As discussed in the text, the κ_2 and κ_4 terms do not contribute to the scattering in our *xy* geometry. Substituting Eq. (4) into Eq. (3), we obtain

$$V = \frac{E^2}{2} \sum_{\langle u,v \rangle} [\kappa_1 (e_x e_x + e_y e_y) + 2\kappa_3 (e_x e_y \operatorname{sgn} \rho_x \operatorname{sgn} \rho_y)] \times (S^+_{u,\alpha} S^-_{v,\beta} + S^-_{u,\alpha} S^+_{v,\beta} + \gamma S^z_{u,\alpha} S^z_{v,\beta}). \tag{B1}$$

By taking the leading terms of the Holstein-Primakoff transformation, we obtain the spin-magnon transformation for simple antiferromagnets

$$\begin{cases} S^+_{u,\alpha} = (2S/N)^{1/2}\sum_{\mathbf{q}} (u_{\mathbf{q}} a_{\downarrow\mathbf{q}} + v_{\mathbf{q}} a^\dagger_{\uparrow-\mathbf{q}})\exp(i\mathbf{q}\cdot\mathbf{r}_u) \\ S^-_{u,\alpha} = (2S/N)^{1/2}\sum_{\mathbf{q}} (u_{\mathbf{q}} a^\dagger_{\downarrow\mathbf{q}} + v_{\mathbf{q}} a_{\uparrow-\mathbf{q}})\exp(-i\mathbf{q}\cdot\mathbf{r}_u) \\ S^+_{v,\beta} = (2S/N)^{1/2}\sum_{\mathbf{q}} (v_{\mathbf{q}} a_{\downarrow-\mathbf{q}} + u_{\mathbf{q}} a^\dagger_{\uparrow\mathbf{q}})\exp(-i\mathbf{q}\cdot\mathbf{r}_v) \\ S^-_{v,\beta} = (2S/N)^{1/2}\sum_{\mathbf{q}} (v_{\mathbf{q}} a^\dagger_{\downarrow-\mathbf{q}} + u_{\mathbf{q}} a_{\uparrow\mathbf{q}})\exp(i\mathbf{q}\cdot\mathbf{r}_v) \\ S^z_{u,\alpha} = S - N^{-1}\sum_{\mathbf{q},\mathbf{q}'} (u_{\mathbf{q}} a^\dagger_{\downarrow\mathbf{q}} + v_{\mathbf{q}} a_{\uparrow-\mathbf{q}})(u_{\mathbf{q}'} a_{\downarrow\mathbf{q}'} + v_{\mathbf{q}'} a^\dagger_{\uparrow-\mathbf{q}'})\exp[i(\mathbf{q}-\mathbf{q}')\cdot\mathbf{r}_u] \\ S^z_{v,\beta} = -S + N^{-1}\sum_{\mathbf{q},\mathbf{q}'} (v_{\mathbf{q}} a_{\downarrow\mathbf{q}} + u_{\mathbf{q}} a^\dagger_{\uparrow-\mathbf{q}})(v_{\mathbf{q}'} a^\dagger_{\downarrow\mathbf{q}'} + u_{\mathbf{q}'} a_{\uparrow-\mathbf{q}'})\exp[-i(\mathbf{q}-\mathbf{q}')\cdot\mathbf{r}_v]. \end{cases} \tag{B2}$$

The interaction Hamiltonian can be expressed in terms of magnon variables. Using

$$\sum_{\mathbf{r}} \exp[-i(\mathbf{q}+\mathbf{q}')\cdot\mathbf{r}] = N\delta_{\mathbf{q},-\mathbf{q}'}, \tag{B3}$$

we obtain

$$\sum_{\langle u,v\rangle} \mathrm{sgn}\,\rho_x\,\mathrm{sgn}\,\rho_y S^+_{u,\alpha} S^-_{v,\beta} = 2S\sum_{\boldsymbol{\rho}}\sum_{\mathbf{q}} (u_{\mathbf{q}} a_{\downarrow\mathbf{q}} + v_{\mathbf{q}} a^\dagger_{\uparrow-\mathbf{q}})(v_{-\mathbf{q}} a^\dagger_{\downarrow\mathbf{q}} + u_{-\mathbf{q}} a_{\uparrow-\mathbf{q}}) \times \mathrm{sgn}\,\rho_x\,\mathrm{sgn}\,\rho_y \exp[-i\mathbf{q}\cdot\boldsymbol{\rho}], \tag{B4}$$

where $\boldsymbol{\rho}$ runs over the eight next-nearest neighbors. Similarly, we have

$$\sum_{\langle u,v\rangle} \mathrm{sgn}\,\rho_x\,\mathrm{sgn}\,\rho_y S^-_{u,\alpha} S^+_{v,\beta} = 2S\sum_{\boldsymbol{\rho}}\sum_{\mathbf{q}} (u_{\mathbf{q}} a^\dagger_{\downarrow\mathbf{q}} + v_{\mathbf{q}} a_{\uparrow-\mathbf{q}})(v_{-\mathbf{q}} a_{\downarrow\mathbf{q}} + u_{-\mathbf{q}} a^\dagger_{\uparrow-\mathbf{q}}) \times \mathrm{sgn}\,\rho_x\,\mathrm{sgn}\,\rho_y \exp[i\mathbf{q}\cdot\boldsymbol{\rho}]. \tag{B5}$$

On substituting Eqs. (B4) and (B5) into Eq. (B1), we can define two trigonometric terms $\Delta^{xy}_{\mathbf{q}}$ and $\Gamma^{xy}_{\mathbf{q}}$ as

$$\sum_{\boldsymbol{\rho}} \mathrm{sgn}(\rho_x)\mathrm{sgn}(\rho_y)\exp(i\mathbf{q}\cdot\boldsymbol{\rho}) = -8\sin(q_x a/2)\sin(q_y a/2)\cos(q_z c/2) \equiv \Delta^{xy}_{\mathbf{q}} \tag{B6}$$

and

$$\sum_{\boldsymbol{\rho}} \exp(i\mathbf{q}\cdot\boldsymbol{\rho}) = \sum_{\boldsymbol{\rho}} \exp(-i\mathbf{q}\cdot\boldsymbol{\rho}) = 8\cos(q_x a/2)\cos(q_y a/2)\cos(q_z c/2) \equiv \Gamma^{xy}_{\mathbf{q}}. \tag{B7}$$

For MnF_2 and FeF_2, the magnon density of states peaks near the Brillouin zone boundary. Note that the term $\Gamma^{xy}_{\mathbf{q}}$ gradually decreases to zero when the magnon wave vector approaches the Brillouin zone boundary. Hence, terms involving $\Gamma^{xy}_{\mathbf{q}}$ give negligible contributions to the two-magnon Raman scattering. On the other hand, the term $\Delta^{xy}_{\mathbf{q}}$ has its maximum value near the M point of the Brillouin zone. Thus terms involving $\Delta^{xy}_{\mathbf{q}}$ dominate the two-magnon scattering. In Eq. (B1), γ is a dimensionless weighting factor related to anisotropy, which is a relatively small effect in the simple antiferromagnets MnF_2 and FeF_2. At the Brillouin zone boundary, with $u_{\mathbf{q}} \approx 1$ and $v_{\mathbf{q}} \approx 0$, we have

$$\sum_{\langle u,v\rangle} \mathrm{sgn}(\rho_x)\mathrm{sgn}(\rho_y)\gamma S^z_{u,\alpha} S^z_{v,\beta} \approx \gamma\sum_{\boldsymbol{\rho}} \mathrm{sgn}(\rho_x)\mathrm{sgn}(\rho_y)\left[-NS^2 + S\sum_{\mathbf{q}} (n_{\uparrow-\mathbf{q}} + n_{\downarrow\mathbf{q}})\right] \equiv 0. \tag{B8}$$

On the other hand,

$$\sum_{\langle u,v\rangle} \kappa_1(e_x e_x + e_y e_y)\gamma S^z_{u,\alpha} S^z_{v,\beta} \approx \kappa_1(e_x e_x + e_y e_y)\gamma\sum_{\boldsymbol{\rho}} \left[-NS^2 + S\sum_{\mathbf{q}} (n_{\uparrow-\mathbf{q}} + n_{\downarrow\mathbf{q}})\right] = \text{const.}, \tag{B9}$$

whose effect is to shift the ground state energy and is not noticeable in spontaneous Raman scattering. Hence it can be neglected, and the only contribution for our light scattering experiment is from the B_{2g} (κ_3) symmetry.

APPENDIX C

With $u_{\mathbf{q}} = u_{-\mathbf{q}} \approx 1$, $v_{\mathbf{q}} = v_{-\mathbf{q}} \approx 0$, $[a_{\downarrow\mathbf{q}}, a_{\uparrow-\mathbf{q}}] = 0$, and $[a^\dagger_{\downarrow\mathbf{q}}, a^\dagger_{\uparrow-\mathbf{q}}] = 0$, we obtain

$$V \approx E^2 \kappa_3 e_x e_y 2S \sum_{\mathbf{q}} \Delta_{\mathbf{q}}^{xy} (a_{\downarrow\mathbf{q}}^{\dagger} a_{\uparrow-\mathbf{q}}^{\dagger} + a_{\downarrow\mathbf{q}} a_{\uparrow-\mathbf{q}}). \quad \text{(C1)}$$

Using $e_x = e_y = \cos(45°) = 1/\sqrt{2}$, Eq. (5) can easily be derived, where we have defined $\Delta_{\mathbf{q}} \equiv \kappa_3 \Delta_{\mathbf{q}}^{xy}$ for convenience; $\Delta_{\mathbf{q}}$ is a coefficient that depends purely on the physical properties of the crystal. Equivalently, we have

$$V_{\mathbf{q}} \approx SE^2 \Delta_{\mathbf{q}} (a_{\downarrow\mathbf{q}}^{\dagger} a_{\uparrow-\mathbf{q}}^{\dagger} + a_{\downarrow\mathbf{q}} a_{\uparrow-\mathbf{q}}), \quad \text{(C2)}$$

with $E^2 \approx (4\pi I / n_R c_L)\delta(t)$.

APPENDIX D

In the Schrödinger picture, Eq. (7) can be derived from Eq. (6) as follows:

$$\begin{aligned}\langle \Psi(t) | (a_{\downarrow\mathbf{q}}^{\dagger} a_{\uparrow-\mathbf{q}}^{\dagger} + a_{\downarrow\mathbf{q}} a_{\uparrow-\mathbf{q}}) | \Psi(t) \rangle &= \langle \Psi(0^+) | e^{-iH_0 t/\hbar} (a_{\downarrow\mathbf{q}}^{\dagger} a_{\uparrow-\mathbf{q}}^{\dagger} + a_{\downarrow\mathbf{q}} a_{\uparrow-\mathbf{q}}) e^{iH_0 t/\hbar} | \Psi(0^+) \rangle \\ &= \langle \Psi(0^-) | \exp\left[i \sum_{\mathbf{q}} \frac{4\pi SI}{n_R c_L \hbar} \Delta_{\mathbf{q}} (a_{\downarrow\mathbf{q}}^{\dagger} a_{\uparrow-\mathbf{q}}^{\dagger} + a_{\downarrow\mathbf{q}} a_{\uparrow-\mathbf{q}}) \right] e^{-iH_0 t/\hbar} (a_{\downarrow\mathbf{q}}^{\dagger} a_{\uparrow-\mathbf{q}}^{\dagger} + a_{\downarrow\mathbf{q}} a_{\uparrow-\mathbf{q}}) e^{iH_0 t/\hbar} \\ &\quad \times \exp\left[-i \sum_{\mathbf{q}} \frac{4\pi SI}{n_R c_L \hbar} \Delta_{\mathbf{q}} (a_{\downarrow\mathbf{q}}^{\dagger} a_{\uparrow-\mathbf{q}}^{\dagger} + a_{\downarrow\mathbf{q}} a_{\uparrow-\mathbf{q}}) \right] | \Psi(0^-) \rangle, \end{aligned} \quad \text{(D1)}$$

where we have $\Psi(0^-) = \Psi_0$, as defined in Eq. (6). In deriving Eq. (7), we have used the following operator identity:

$$e^B X e^{-B} = X + [B,X] + \frac{1}{2!}[B,(B,X)] + \cdots + \frac{1}{n!}\{B,[B,\ldots,(B,X)\ldots]\} + \cdots. \quad \text{(D2)}$$

APPENDIX E

Noting that

$$S_{l,\alpha}^{+} S_{l,\beta}^{-} + S_{l,\alpha}^{-} S_{l,\beta}^{+} = 2(S_{l,\alpha}^{x} S_{l,\beta}^{x} + S_{l,\alpha}^{y} S_{l,\beta}^{y}), \quad \text{(E1)}$$

we derive for the local magnetization

$$\langle \mathbf{m}_l \cdot \mathbf{m}_l \rangle = (g\mu_B)^2 [2S(S+1) + \langle S_{l,\alpha}^{+} S_{l,\beta}^{-} + S_{l,\alpha}^{-} S_{l,\beta}^{+} \rangle + 2\langle S_{l,\alpha}^{z} S_{l,\beta}^{z} \rangle]. \quad \text{(E2)}$$

We next consider magnons near the Brillouin zone boundary M point in Eq. (B2), which yields

$$\sum_{l} \langle S_{l,\alpha}^{+} S_{l,\beta}^{-} + S_{l,\alpha}^{-} S_{l,\beta}^{+} \rangle = -2S \sum_{\mathbf{q}} \langle a_{\downarrow\mathbf{q}}^{\dagger} a_{\uparrow-\mathbf{q}}^{\dagger} + a_{\downarrow\mathbf{q}} a_{\uparrow-\mathbf{q}} \rangle(t). \quad \text{(E3)}$$

From Eq. (7), under the low-intensity limit, we know that

$$\sum_{l} \langle S_{l,\alpha}^{+} S_{l,\beta}^{-} + S_{l,\alpha}^{-} S_{l,\beta}^{+} \rangle = \frac{16\pi IS^2}{n_R c_L \hbar} \sum_{\mathbf{q}} \Delta_{\mathbf{q}} \sin(2\Omega_{\mathbf{q}} t). \quad \text{(E4)}$$

At the same time, we have

$$\sum_{l} 2\langle S_{l,\alpha}^{z} S_{l,\beta}^{z} \rangle = -2NS^2 + 2S \sum_{\mathbf{q}} \langle a_{\downarrow\mathbf{q}}^{\dagger} a_{\downarrow\mathbf{q}} + a_{\uparrow-\mathbf{q}}^{\dagger} a_{\uparrow-\mathbf{q}} \rangle(t) \approx -2NS^2. \quad \text{(E5)}$$

Hence, in the low-intensity limit,

$$\frac{1}{2} \sum_{l} \langle \mathbf{m}_l^2 \rangle / (g\mu_B)^2 = NS + \frac{8\pi IS^2}{n_R c_L \hbar} \sum_{\mathbf{q}} \Delta_{\mathbf{q}} \sin(2\Omega_{\mathbf{q}} t). \quad \text{(E6)}$$

Note that $\langle \mathbf{m}_l^2 \rangle$ has the same value for all cells, and that $\langle \mathbf{m}_l \rangle = 0$ always. Thus we readily derive Eq. (9).

APPENDIX F

Given the polarization configuration in Fig. 7 and the Raman tensors of B_{2g} and A_{1g} symmetries shown in Appendix A, we have after some calculations,

$$\Delta I(B_{2g}) \propto e^2 \sin(2\theta)\sin[2(\theta+\gamma)],$$

$$\Delta I(A_{1g}) \propto a^2. \quad \text{(F1)}$$

In our experiment, $\theta = \pi/4$. If we set $\gamma = \pi/4$, we have $\Delta I(B_{2g}) = 0$. However, if we decompose the probe beam along the two directions that are parallel to, or perpendicular to, the pump beam, we have for $\gamma = 0$, $\Delta I(B_{2g}) \propto e^2$, and for $\gamma = \pi/2$, $\Delta I(B_{2g}) \propto -e^2$. Thus,

$$\Delta I(B_{2g})|_{\gamma=0} - \Delta I(B_{2g})|_{\gamma=\pi/2} \propto 2e^2, \quad \text{(F2)}$$

which gives the differential transmission for B_{2g} symmetry. A similar estimation for A_{1g} symmetry shows that it should be eliminated by this detection method.

*Present address: Laboratory for Photonics & Quantum Electronics, 192 IATL, University of Iowa, Iowa City, Iowa 52242, USA.
†Present address: Departamento de Fisica, FCEyN, Universidad de Buenos Aires, 1428 Buenos Aires, Argentina.
‡Email address: david.lockwood@nrc.ca

[1] W. Heisenberg, Z. Phys. **43**, 172 (1927).
[2] D. F. Walls and G. J. Milburn, *Quantum Optics* (Springer-Verlag, Berlin, 1994).
[3] R. E. Slusher, L. W. Hollberg, B. Yurke, J. C. Mertz, and J. F. Valley, Phys. Rev. Lett. **55**, 2409 (1985).
[4] R. Loudon and P. L. Knight, J. Mod. Opt. **34**, 709 (1987).
[5] L. Davidovich, Rev. Mod. Phys. **68**, 127 (1996).
[6] T. J. Dunn, J. N. Sweetser, I. A. Walmsley, and C. Radzewicz, Phys. Rev. Lett. **70**, 3388 (1993).
[7] G. A. Garrett, A. G. Rojo, A. K. Sood, J. F. Whitaker, and R. Merlin, Science **275**, 1638 (1997).
[8] G. A. Garrett, J. F. Whitaker, A. K. Sood, and R. Merlin, Opt. Express **1**, 385 (1997).
[9] A. Bartels, T. Dekorsy, and H. Kurz, Phys. Rev. Lett. **84**, 2981 (2000).
[10] A. G. Stepanov, J. Hebling, and J. Kuhl, Phys. Rev. B **63**, 104304 (2001).
[11] A. Kuzmich, L. Mandel, and N. P. Bigelow, Phys. Rev. Lett. **85**, 1594 (2000).
[12] J. Hald, J. L. Sørensen, C. Schori, and E. S. Polzik, Phys. Rev. Lett. **83**, 1319 (1999).
[13] D. J. Wineland, J. J. Bollinger, W. M. Itano, and D. J. Heinzen, Phys. Rev. A **50**, 67 (1994).
[14] B. Julsgaard, A. Kozhekin, and E. S. Polzik, Nature **413**, 400 (2001).
[15] A. Dantan, M. Pinard, V. Josse, N. Nayak, and P. R. Berman, Phys. Rev. A **67**, 045801 (2003).
[16] Xiaoguang Wang and B. C. Sanders, Phys. Rev. A **68**, 012101 (2003).
[17] B. Yurke, P. G. Kaminsky, R. E. Miller, E. A. Whittaker, A. D. Smith, A. H. Silver, and R. W. Simon, Phys. Rev. Lett. **60**, 764 (1988).
[18] M. G. Cottam and D. J. Lockwood, *Light Scattering in Magnetic Solids* (Wiley, New York, 1986).
[19] Jimin Zhao, A. V. Bragas, D. J. Lockwood, and R. Merlin, Phys. Rev. Lett. **93**, 107203 (2004).
[20] A. P. Mayer, R. K. Wehner, and A. A. Maradudin, Phys. Rev. B **62**, 5513 (2000), and references therein.
[21] P. A. Fleury and R. Loudon, Phys. Rev. **166**, 514 (1968).
[22] A. Okazaki, K. C. Turberfield, and R. W. H. Stevenson, Phys. Lett. **8**, 9 (1964).
[23] C. Kittel, *Quantum Theory of Solids* (Wiley, New York, 1987).
[24] D. J. Lockwood and M. G. Cottam, Phys. Rev. B **35**, 1973 (1987).
[25] D. J. Lockwood, in *Raman Scattering in Materials Science*, edited by W. H. Weber and R. Merlin (Springer, New York, 2000), p. 230.
[26] R. Merlin, Solid State Commun. **102**, 207 (1997).
[27] S. P. S. Porto, P. A. Fleury, and T. C. Damen, Phys. Rev. **154**, 522 (1967).
[28] M. G. Cottam, V. So, D. J. Lockwood, R. S. Katiyar, and H. J. Guggenheim, J. Phys. C **16**, 1741 (1983).
[29] H. Barkhuijsen, R. de Beer, W. M. M. J. Bovée, and D. van Ormondt, J. Magn. Reson. (1969-1992) **61**, 465 (1985).
[30] F. W. Wise, M. J. Rosker, G. L. Millhauser, and C. L. Tang, IEEE J. Quantum Electron. **23**, 1116 (1987).
[31] Taiju Tsuboi and P. Ahmet, Phys. Rev. B **45**, 468 (1992).
[32] T. E. Stevens, J. Kuhl, and R. Merlin, Phys. Rev. B **65**, 144304 (2002).
[33] See EPAPS Document No. E-PRBMDO-73-079618 for a movie depicting magnon squeezing. This document can be reached via a direct link in the online article's HTML reference section or via the EPAPS homepage (http://www.aip.org/pubservs/epaps.html).
[34] M. G. Cottam and D. J. Lockwood, Phys. Rev. B **31**, 641 (1985).
[35] D. J. Lockwood and M. G. Cottam, J. Appl. Phys. **64**, 5876 (1988).